Geochemical Perspectives Letters

Sulfur and mercury MIF suggest volcanic contributions to Earth's atmosphere at 2.7 Ga

A.L. Zerkle[1*], M.W. Claire[1], T. Di Rocco[1,2], N.V. Grassineau[3], E.G. Nisbet[3], R. Sun[4], R. Yin[4*]

OPEN ACCESS
doi: 10.7185/geochemlet.2124

Abstract

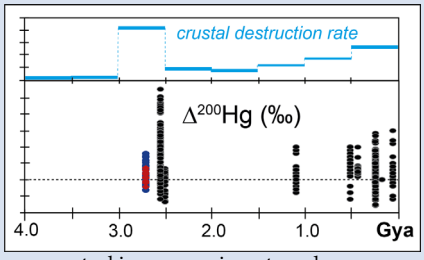

The Archean eon is associated with large-scale changes in Earth's geosphere and biosphere, including the onset of plate tectonics and the expansion of oxygenic photosynthesis, although the full impacts of these changes on the atmosphere remain unclear. Here we present coupled records of mass independent fractionation of sulfur (S-MIF) and mercury (Hg-MIF) isotopes from well preserved sediments of the ~2.7 billion year old (Ga) Manjeri Formation, Belingwe Greenstone Belt, Zimbabwe. These palaeoatmospheric proxies record different trends for S-MIF and odd number Hg-MIF *versus* even number Hg-MIF, providing novel constraints on atmospheric chemistry during this time. S-MIF and odd number Hg-MIF values are muted in comparison to values preserved in later Archean sediments, representing a combination of enhanced volcanic input and local mixing. Even number Hg-MIF is absent from these sediments, consistent with complete photo-oxidation of gaseous Hg^0, which could have been driven by increased halogen emissions from arc volcanism. When considered within a global geodynamic context, these MIF data suggest an important role for subduction zone-related volcanism associated with early plate tectonics in modulating the ~2.7 Ga atmosphere.

Received 5 May 2021 | Accepted 16 August 2021 | Published 9 September 2021

Introduction

The mid- to late-Archean, between ~3.2 and 2.5 billion years ago (Gyr), was a time of great transitions in Earth history, including the evolutionary proliferation of cyanobacteria performing oxygenic photosynthesis (Farquhar *et al.*, 2011; Nisbet and Fowler, 2014) and the development of plate tectonics (Hawkesworth *et al.*, 2020). Both of these events would have fundamentally altered Earth's surface environments and planetary habitability, the former by introducing a strong oxidant, and the latter by modulating fluxes of carbon and other volatile elements between the mantle and the surface (Zerkle, 2018). Although geosphere-biosphere-atmosphere feedbacks would have been essential in driving (and responding to) these critical changes in Earth's history, geochemical markers that place direct constraints on atmospheric evolution during this time period remain elusive.

Mass independent fractionation of sulfur isotopes (S-MIF) provide vital clues into past atmospheric chemistry. The presence of large magnitude S-MIF in rocks deposited prior to ~2.43 Ga provides compelling evidence for an oxygen-poor atmosphere in the Archean and early Palaeoproterozoic (Farquhar *et al.*, 2000; Warke *et al.*, 2020). The S-MIF record also displays significant variations in magnitude, sign, and quadruple S isotope systematics (expressed as $\Delta^{33}S$ and $\Delta^{36}S$; Eqs. S-2, S-3) that could provide additional constraints on Earth's reducing atmosphere. In particular, a decrease in the magnitude of S-MIF has been reported in Archean rocks deposited between ~3.2 and 2.7 Ga (Fig. 1). This "mid-Archean MIF minimum" has been variably attributed to changes in global atmospheric chemistry, which could shield or dampen S-MIF forming reactions (Farquhar *et al.*, 2007; Domagal-Goldman *et al.*, 2008; Kurzweil *et al.*, 2013; Liu *et al.*, 2019), or to dilution or mixing of atmospheric sulfur sources on a local or regional scale (Guy *et al.*, 2012; Thomazo *et al.*, 2013; Marin-Carbonne *et al.*, 2014).

MIF of mercury (Hg) isotopes in marine sediments can provide additional constraints on atmospheric chemistry. Mercury undergoes MIF of both odd number isotopes (expressed as $\Delta^{199}Hg$ and $\Delta^{201}Hg$; Eq. S-5) and even number isotopes (expressed as $\Delta^{200}Hg$) during Hg transformations between the atmosphere and oceans (Blum *et al.*, 2014). Odd number Hg-MIF is predominatly produced by photo-reduction of aqueous Hg^{2+}, which occurs mainly in the surface ocean but also in rain droplets (Bergquist and Blum, 2007). By contrast, even number Hg-MIF is only produced during gas phase Hg^0 photo-oxidation in the atmosphere (Cai and Chen, 2016). In the oceans, MIF-bearing Hg complexes with organic matter and sulfur ligands and is deposited in the sediments. The resulting Hg-MIF signals are robust to post-depositional alteration (Grasby *et al.*, 2016) and can record additional, complementary atmospheric constraints (Zerkle *et al.*, 2020). Here we present coupled records

1. School of Earth and Environmental Sciences and Centre for Exoplanet Science, University of St Andrews, St Andrews, Fife, KY16 9AL, Scotland, UK
2. Current address: Geowissenschaftliches Zentrum, Universität Göttingen, 37077 Göttingen, Germany
3. Department of Earth Sciences, Royal Holloway, University of London, Egham TW20 OEX, UK
4. State Key Laboratory of Ore Deposit Geochemistry, Institute of Geochemistry, Chinese Academy of Sciences, Guiyang 550081, China
* Corresponding author (email: az29@st-andrews.ac.uk, yinrunsheng@mail.gyig.ac.cn)

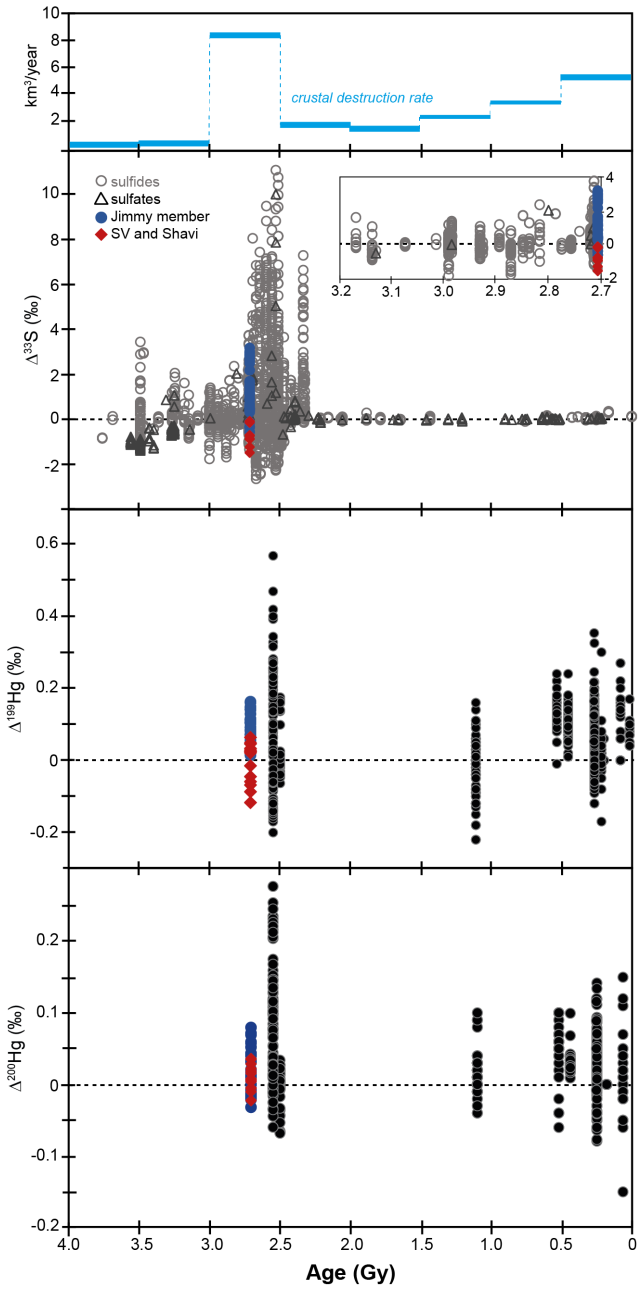

Figure 1 Temporal trends in S-MIF and Hg-MIF through time (updated from Farquhar *et al.*, 2014, and Zerkle *et al.*, 2020). Crustal destruction rates are modelled for 500 million year bins (Dhuime *et al.*, 2018).

of S-MIF and Hg-MIF data from well preserved sediments of the ~2.7 Ga Manjeri Formation of the Belingwe Greenstone Belt, Zimbabwe, to determine local *versus* global controls on MIF records, and to unravel drivers of Archean atmospheric chemistry.

Sulfur and Mercury MIF in the Manjeri Formation

Our samples were collected from three drill cores through the ~2.7 Ga Manjeri Formation (Fm) of the Belingwe Greenstone Belt, Zimbabwe (as detailed in Yang *et al.*, 2019, and SI). This section of the Manjeri Fm (Hunter *et al.*, 1998) records a marine transgression from a basal unconformity and the intertidal facies of the Spring Valley (SV) member, through the subtidal Shavi member (preserved in the NERCMAR core) to the deeper water shales of the Jimmy member (preserved in cores A and B).

S-MIF from the Manjeri Fm had $\Delta^{33}S$ values ranging from -1.5 to +3.1 ‰, with positive $\Delta^{33}S$ values dominating the Jimmy member and negative $\Delta^{33}S$ values dominating the Spring Valley and Shavi members (Fig. 2). These S-MIF values are larger in magnitude than bulk rock $\Delta^{33}S$ values previously reporteded from ~2.7 Ga (*e.g.*, Thomazo *et al.*, 2013), but still significantly smaller than $\Delta^{33}S$ values preserved in ~2.5 Ga sediments (Fig. 1). Shielding of S-MIF forming reactions by oxygen or organic haze have been proposed to erase or decrease S-MIF (Domagal-Goldman *et al.*, 2008; Kurzweil *et al.*, 2013; Liu *et al.*, 2019), but the persistence of S-MIF in these samples precludes an ozone layer, and the $\Delta^{36}S$-$\Delta^{33}S$ dynamics are inconsistent with haze formation (Fig. 2b) (Zerkle *et al.*, 2012). Modelling studies have shown that higher total volcanic sulfur fluxes can alter sulfur exit channels and decrease S-MIF values (Claire *et al.*, 2014), providing one potential explanation for lower magnitude atmospheric S-MIF.

Local- or basinal-scale mixing of primary atmospheric S sources can further dampen sedimentary S-MIF signals (*e.g.*, Marin-Carbonne *et al.*, 2014). Following mass balance, the preservation of S-MIF in ancient sediments requires two or more exit channels for atmospheric sulfur, conventionally considered to be elemental sulfur carrying a positive $\Delta^{33}S$ signature (as seen in the Jimmy member) and sulfate carrying a negative $\Delta^{33}S$ signal (as seen in the SV and Shavi members), although this remains debated (Claire *et al.*, 2014; Harman *et al.*, 2018). In particular, the very small S-MIF in some samples from the Jimmy member (with $\Delta^{33}S < 2$ ‰) could reflect further muting of primary atmospheric S-MIF values *via* mixing. Mixing could have been driven by biological processes (*e.g.*, through re-oxidation of reduced S), physical processes (*e.g.*, mixing of Fe-sulfides derived from sulfate reduction with polysulfides to form pyrite), or some combination of both (Fig. 2a). Previous studies indicate that Jimmy member sediments supported an active biogeochemical S cycle in proximity to a redox interface (Yang *et al.*, 2019), consistent with this interpretation.

Mercury isotopes provide new insights into environmental conditions during deposition of the Manjeri strata. $\delta^{202}Hg$ values alone are difficult to interpret, since mass dependent fractionation of Hg occurs during all Hg cycling processes (Blum *et al.*, 2014). In contrast, mercury MIF provides clearer constraints on atmospheric Hg cycling, as it mainly occurs during photon-mediated processes with little contribution from biogeochemical cycling, and even number Hg-MIF is produced exclusively in the atmosphere. Odd number Hg-MIF from the Manjeri Fm support two sources of Hg to the sediments, one dominated by positive odd number Hg-MIF, and one dominated by negative odd number Hg-MIF (Fig. 2c). In the modern environment, rain and open marine samples that mainly contain Hg^{2+} species are characterised by positive odd number Hg-MIF (*e.g.*, Štrok *et al.*, 2015), while terrestrial reservoirs and modern coastal sediments that primarily accumulate Hg^0 are characterised by negative odd number Hg-MIF (Blum *et al.*, 2014). These Hg-MIF values therefore suggest that the dominant source of Hg to the SV and Shavi members was Hg^0 species deposited in a shallow depositional environment, where enhanced terrestrial nutrient input stimulated local primary productivity, driving near shore anoxia. The Jimmy member, on the other hand, was dominated by Hg^{2+} species deposited in a more oligotrophic open ocean environment, adjacent to a deeper water chemocline. This depositional scenario is supported by previously published sedimentology (Hunter *et al.*, 1998) and ocean redox data from these same cores (Yang *et al.*, 2019). Combined S-MIF and

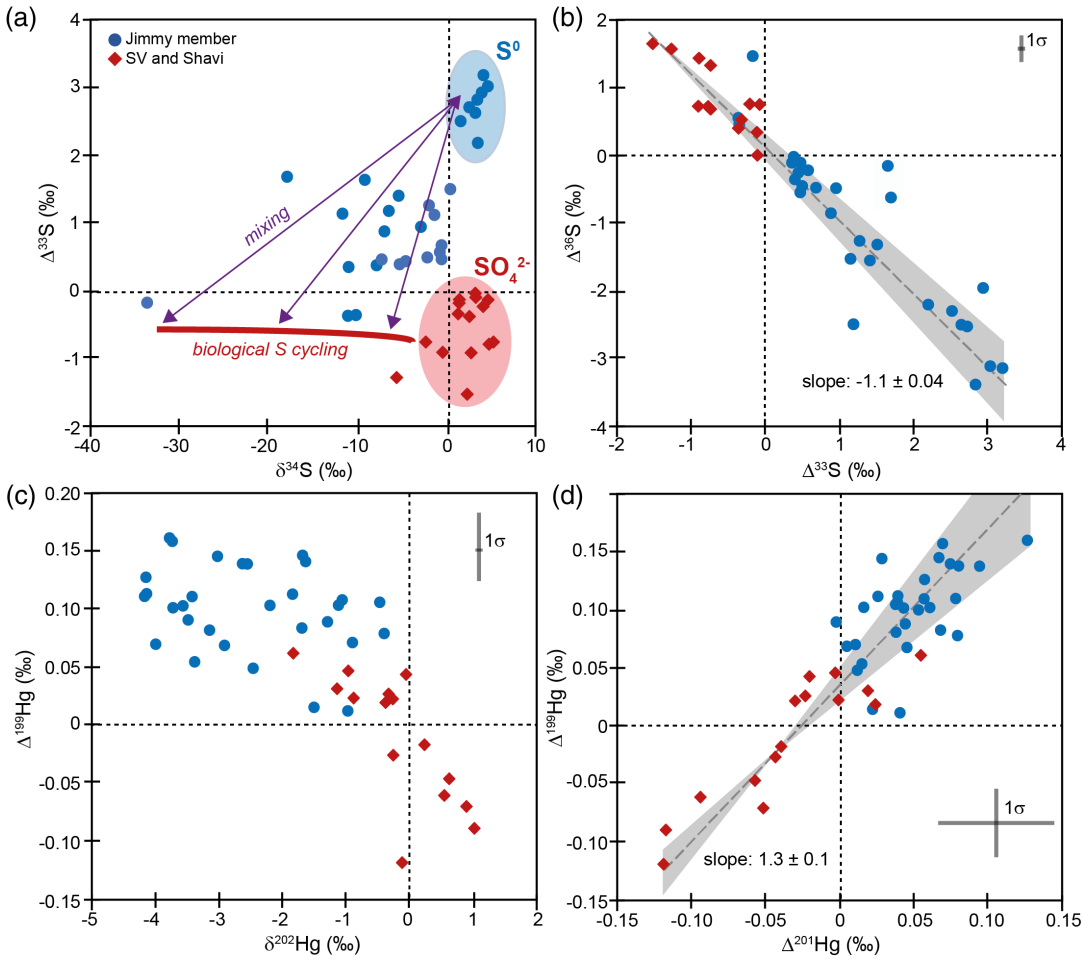

Figure 2 **(a-d)** Cross plots of S-MIF and Hg-MIF values. Panel **(a)** includes interpretations of S-MIF based on the conventional view of sulfur exit channels (but see Harman *et al.*, 2018, for an alternative view). Panels **(b)** and **(d)** include orthogonal data regressions, showing the calculated linear slopes (gray dashed line) and 3σ confidence intervals (gray blue area). The $\Delta^{36}S/\Delta^{33}S$ slope is consistent with the Archean reference array (Ono *et al.*, 2009); the $\Delta^{199}Hg/\Delta^{201}Hg$ slope is consistent with production of odd number Hg-MIF during Hg^{2+} photo-reduction (Bergquist and Blum, 2007).

Hg-MIF data also indicate that the atmospheric exit channel carrying a negative $\Delta^{33}S$ signal dominated the S pool in shallow, near shore environments, while atmospheric S carrying a positive $\Delta^{33}S$ signal dominated in open ocean environments (Fig. 3).

Similar to S-MIF, Hg-MIF values from the 2.7 Ga Belingwe strata are muted (odd number Hg-MIF) or completely absent (even number Hg-MIF) in comparison to Hg-MIF data from the later Archean (Fig. 1). A decrease in the magnitude of sedimentary Hg-MIF towards values of 0 ‰ is generally attributed to enhanced atmospheric flux of vocanically-derived Hg^0 to the sediments, since volcanic Hg^0 has $\Delta^{199}Hg$ and $\Delta^{200}Hg$ values of 0 ‰ (Zambardi *et al.*, 2009). Ratios of mercury to TOC in the Manjeri Fm support high volcanic Hg^0 inputs to the sediments, particularly in the near shore SV and Shavi members (1274 ± 584 ppb Hg/wt. % TOC; Grasby *et al.*, 2019). However, volcanic Hg^0 input would affect both odd number and even number Hg-MIF similarly, as would any post-depositional mixing processes, so neither of these mechanisms can explain the entirety of our Hg-MIF data.

The complete absence of even number Hg-MIF in these sediments instead requires further alteration of the photo-oxidation processes that uniquely produce $\Delta^{200}Hg$ anomalies. The dominant oxidation pathway for Hg^0 in the modern atmosphere is reaction with halogens, such as bromine and chlorine (Dibble *et al.*, 2020), and these reactions have been shown to produce

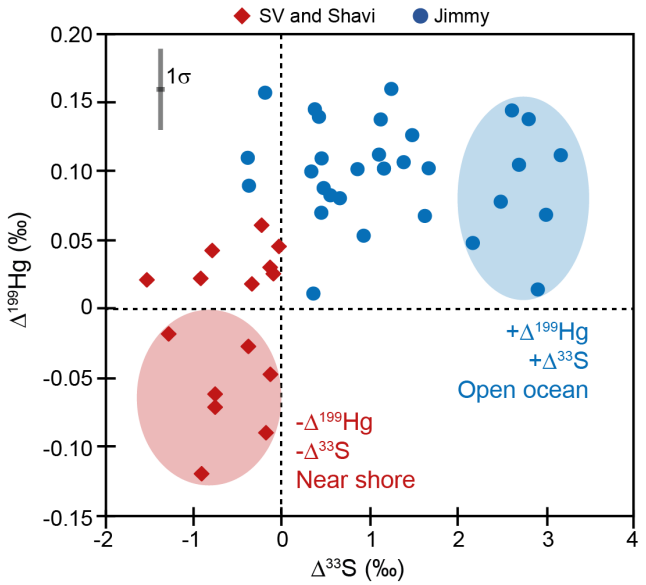

Figure 3 Trends in S-MIF *versus* Hg-MIF, with associated interpretations based on comparison with modern sedimentary Hg-MIF values.

even number Hg-MIF (Sun *et al.*, 2016). In the modern Earth system, the largest volcanic source of halogens is from subduction zone-related arc volcanism (Pyle and Mather, 2009). Enhanced volcanic fluxes of SO_2 and halogens into the atmosphere could have driven Hg^0 photo-oxidation reactions near to completion, as seen with seasonal atmospheric mercury depletion events that occur in modern polar regions (Carignan and Sonke, 2010), erasing any even number Hg-MIF signal. Halogens could have additionally been supplied from komatiitic volcanism, as indicated by the overlying Zeederbers Fm deposited several million years later (Cameron *et al.*, 1979).

Enhanced global volcanic gas fluxes could have contributed both MIF-free sulfur and mercury to the sediments, diluting the overall magnitudes of sedimentary MIF. In addition, the complete lack of even number Hg-MIF in these sediments suggests a volcanic source rich in halogens, similar to modern arc volcanism. Therefore, enhanced arc volcanism provides the only self-consistent mechanism that can reconcile all three sets of MIF records. Within a global geodynamic context, models of continental crust formation suggest that crustal destruction rates increased dramatically at ~3.0 Ga, inferred to represent the widespread development of subduction zones (Fig. 1) (Dhuime *et al.*, 2018). The increase in crustal destruction rates, coupled with the development and amalgamation of Archean supercontinents, are taken to reflect the onset of plate tectonics as the dominant global regime during this time (Hawkesworth *et al.*, 2020). Our data are consistent with enhanced volatile fluxes from subduction zone arc volcanism at ~2.7 Ga. Following this scenario, the increase in S-MIF and Hg-MIF between 2.7 and 2.5 Ga could be explained by decreased volcanic emissions during the transition to tectonic quiescence in the Palaeoproterozoic (Cawood and Hawkesworth, 2014). As a corollary, the time span of the mid-Archean S-MIF minimum could indicate that volcanic emissions from plate tectonics exerted a fundamental control on atmospheric chemistry from ~3.2 to 2.7 Ga, before biology wrested control in the ensuing ~200 million years (*e.g.*, Kurzweil *et al.*, 2013; Izon *et al.*, 2017).

Acknowledgements

This study received funding from a Natural Environment Research Council Standard Grant NE/M001156/1 (ALZ, EGN), and from the European Research Council under the European Union's Horizon 2020 research and innovation programme (Grant 678812 to MWC). RS and RY were supported by the Natural Science Foundation of China (41873047).

Editor: Gavin Foster

Additional Information

Supplementary Information accompanies this letter at https://www.geochemicalperspectivesletters.org/article2124.

Cite this letter as: Zerkle, A.L., Claire, M.W., Di Rocco, T., Grassineau, N.V., Nisbet, E.G., Sun, R., Yin, R. (2021) Sulfur and mercury MIF suggest volcanic contributions to Earth's atmosphere at 2.7 Ga. *Geochem. Persp. Let.* 18, 48–52.

References

Bergquist, B.A., Blum, J.D. (2007) Mass-dependent and -independent fractionation of Hg isotopes by photoreduction in aquatic systems. *Science* 318, 417–420.

Blum, J.D., Sherman, L.S., Johnson, M.W. (2014) Mercury isotopes in earth and environmental sciences. *Annual Review of Earth and Planetary Sciences* 42, 249–269.

Cai, H.M., Chen, J.B. (2016) Mass-independent fractionation of even mercury isotopes. *Science Bulletin* 61, 116–124.

Cameron, W.E., Nisbet, E.G., Dietrich, V.J. (1979) Boninites, komatiites, and ophiolitic basalts. *Nature* 280.

Carignan, J., Sonke, J.E. (2010) The effect of atmospheric mercury depletion events on the net deposition flux around Hudson Bay, Canada. *Atmospheric Environment* 44, 4372–4379.

Cawood, P.A., Hawkesworth, C.J. (2014) Earth's middle age. *Geology* 42, 503–506.

Claire, M.W., Kasting, J.F., Domagal-Goldman, S.D., Stueken, E.E., Buick, R., Meadows, V.S. (2014) Modeling the signature of sulfur mass-independent fractionation produced in the Archean atmosphere. *Geochimica et Cosmochimica Acta* 141, 365–380.

Dhuime, B., Hawkesworth, C.J., Delavault, H., Cawood, P.A. (2018) Rates of generation and destruction of the continental crust: implications for continental growth. *Philosophical Transactions of the Royal Society A* 376.

Dibble, T.S., Tetu, H.L., Jiao, Y.G., Thackray, C.P., Jacob, D.J. (2020) Modeling the OH-Initiated Oxidation of Mercury in the Global Atmosphere without Violating Physical Laws. *Journal of Physical Chemistry A* 124, 444–453.

Domagal-Goldman, S.D., Kasting, J.F., Johnston, D.T., Farquhar, J. (2008) Organic haze, glaciations and multiple sulfur isotopes in the Mid-Archean Era. *Earth and Planetary Science Letters* 269, 29–40.

Farquhar, J., Bao, H.M., Thiemens, M. (2000) Atmospheric influence of Earth's earliest sulfur cycle. *Science* 289, 756–758.

Farquhar, J., Peters, M., Johnston, D.T., Strauss, H., Masterson, A., Wiechert, U., Kaufman, A.J. (2007) Isotopic evidence for Mesoarchaean anoxia and changing atmospheric sulphur chemistry. *Nature* 449, 706–709.

Farquhar, J., Zerkle, A.L., Bekker, A. (2011) Geological constraints on the origin of oxygenic photosynthesis. *Photosynthesis Research* 107, 11–36.

Farquhar, J., Zerkle, A.L., Bekker, A. (2014) 6.4 - Geologic and Geochemical Constraints on the Earth's Early Atmosphere. In: Holland, H.D., Turekian, K.K. (Eds.) *Treatise on Geochemistry*. Second Edition, Elsevier, Oxford, 91–138.

Grasby, S.E., Shen, W., Yin, R., Gleason, J.D., Blum, J.D., Lepak, R.F., Hurley, J.P., Beauchamp, B. (2016) Isotopic signatures of mercury contamination in latest Permian oceans. *Geology* 45, 55–58.

Grasby, S.E., Them II, T.R., Chen, Z., Yin, R., Ardakani, O.H. (2019) Mercury as a proxy for volcanic emmisions in the geologic record. *Earth Science Reviews* 196, 102880.

Guy, B.M., Ono, S., Gutzmer, J., Kaufman, A., Lin, Y., Fogel, M., Beukes, N. (2012) A multiple sulfur and organic carbon isotope record from non-conglomeratic sedimentary rocks of the Mesoarchean Witwatersrand Supergroup, South Africa. *Precambrian Research* 216-219, 208–231.

Harman, C.E., Pavlov, A., Babikov, D., Kasting, J.F. (2018) Chain formation as a mechanism for mass-independent fractionation of sulfur isotopes in the Archean atmosphere. *Earth and Planetary Science Letters* 496, 238–247.

Hawkesworth, C.J., Cawood, P.A., Dhuime, B. (2020) The evolution of the continental crust and the onset of plate tectonics. *Frontiers in Earth Science* 8.

Hunter, M.A., Bickle, M.J., Nisbet, E.G., Martin, A., Chapman, H.J. (1998) Continental extensional setting for the Archean Belingwe Greenstone Belt, Zimbabwe. *Geology* 26, 883–886.

Izon, G., Zerkle, A.L., Williford, K.H., Farquhar, J., Poulton, S.W., Claire, M.W. (2017) Biological regulation of atmospheric chemistry en route to planetary oxygenation. *PNAS* 114, 2571–2579.

Kurzweil, F., Claire, M.W., Thomazo, C., Peters, M., Hannington, M.D., Strauss, H. (2013) Atmospheric sulfur rearrangement 2.7 billion years ago: Evidence for oxygenic photosynthesis. *Earth and Planetary Science Letters* 366, 17–26.

Liu, P., Harman, C.E., Kasting, J.F., Hu, Y., Wang, J. (2019) Can organic haze and O2 plumes explain patterns of sulfur mass-independent fractionation during the Archean? *Earth and Planetary Science Letters* 526, 115767.

Marin-Carbonne, J., Rollion-Bard, C., Bekker, A., Rouxel, O., Agangi, A., Cavalazzi, B., Wohlgemuth-Ueberwasser, C.C., Hofmann, A., McKeegan, K.D. (2014) Coupled Fe and S isotope variations in pyrite nodules from Archean shale. *Earth and Planetary Science Letters* 392, 67–79.

Nisbet, E.G., Fowler, C.M.R. (2014) 10.1 - The Early History of Life. In: Holland, H.D., Turekian, K.K. (Eds.) *Treatise on Geochemistry*. Second Edition, Elsevier, Oxford, 1–42.

Ono, S., Beukes, N.J., Rumble, D. (2009) Origin of two distinct multiple-sulfur isotope compositions of pyrite in the 2.5 Ga Klein Naute Formation, Griqualand West Basin, South Afric. *Precambrian Research* 169, 48–57.

Pyle, D.M., Mather, T.A. (2009) Halogens in igneous processes and their fluxes to the atmosphere and oceans from volcanic activity: A review. *Chemical Geology* 263, 110–121.

Štrok, M., Baya, P.A., Hintelmann, H. (2015) The mercury isotope composition of Arctic coastal seawater. *Comptes Rendus Geoscience* 347, 368–376.

Sun, G., Sommar, J., Feng, X., Lin, C.-J., Ge, M., Wang, W., Yin, R., Fu, X., Shang, L. (2016) Mass-dependent and independent fractionation of mercury isotopes during gas-phase oxidation of elemental mercury vapor by atomic Cl and Br. *Environmental Science & Technology* 50, 9232–9241.

Thomazo, C., Grassineau, N.V., Nisbet, E.G., Peters, M., Strauss, H. (2013) Multiple sulfur and carbon isotope composition of sediments from the Belingwe Greenstone Belt (Zimbabwe): A biogenic methane regulation on mass independent fractionation of sulfur during the Neoarchean? *Geochimica et Cosmochimica Acta* 121, 120–138.

Warke, M.R., Di Rocco, T., Zerkle, A.L., Lepland, A., Prave, A.R., Martin, A., Ueno, Y., Condon, D.J., Claire, M. (2020) The Great Oxidation Event preceded a Paleoproterozoic "snowball Earth". *PNAS* 117, 13314–13320.

Yang, J., Junium, C.K., Grassineau, N.V., Nisbet, E.G., Izon, G., Mettam, C., Martin, A., Zerkle, A.L. (2019) Ammonium availability in the Late Archaean nitrogen cycle. *Nature Geoscience* 12, 553–557.

Zambardi, T., Sonke, J.E., Toutain, J.P., Sortino, F., Shinohara, H. (2009) Mercury emissions and stable isotopic compositions at Vulcano Island (Italy). *Earth and Planetary Science Letters* 277, 236–243.

Zerkle, A.L. (2018) Biogeodynamics: bridging the gap between surface and deep Earth processes. *Philosophical Transactions of the Royal Society A* 376, 20170401.

Zerkle, A.L., Claire, M.W., Domagal-Goldman, S.D., Farquhar, J., Poulton, S.W. (2012) A bistable organic-rich atmosphere on the Neoarchean Earth. *Nature Geoscience* 5, 359–363.

Zerkle, A.L., Yin, R., Chen, C., Li, X., Izon, G., Grasby, S. (2020) Anomalous fractionation of mercury isotopes in the Late Archean atmosphere. *Nature Communications* 11, 1709.

Geochemical Perspectives Letters

Sulfur and mercury MIF suggest volcanic contributions to Earth's atmosphere at 2.7 Ga

A.L. Zerkle, M.W. Claire, T. Di Rocco, N.V. Grassineau, E.G. Nisbet, R. Sun, R. Yin

Supplementary Information

The Supplementary Information includes:

- Materials and Methods
- Tables S-1 to S-3
- Figures S-1 and S-2
- Supplementary Information References

Materials and Methods

Our samples were collected from three drill cores through the ~2.7 Ga Manjeri Formation (Fm) of the Belingwe Greenstone Belt in Zimbabwe (Fig. S-1). This section of the Manjeri Fm records a marine transgression from the intertidal facies of the Spring Valley member and subtidal Shavi member to the exceptionally well-preserved shales of the Jimmy member. Sedimentary textures imply that the Jimmy member was deposited in a deeper shelf setting below wave base (Grassineau *et al.*, 2006). Lead-lead isochrons derived from stromatolites of the Manjeri Fm indicate a depositional age of 2.706 ± 0.049 Ga (Bolhar *et al.*, 2002). Overall, the metamorphic grade of the studied succession is remarkably low for rocks of this age, as supported by the preservation of texturally pristine and mineralogically unaltered komatiites (Nisbet *et al.*, 1987). The studied drill cores, NERCMAR, Core A and Core B, were taken from the eastern margin of the Belingwe belt (Fig. S-1, S-2), where the Manjeri Fm unconformably overlies much older gneissic crust. The detailed geological setting and stratigraphy of the NERCMAR drill core, which intersects the entirety of the Manjeri Fm, was described in Grassineau *et al.* (2006). Cores A and B, which recovered extensive sections of the Jimmy member, were described in detail by Yang *et al.* (2019).

Sulfide extractions were performed in the Geobiology Lab at the University of St Andrews using the chromium reduction method, as described previously (Izon *et al.*, 2015). Major sulfur isotope analyses ($\delta^{34}S$) were performed on the resulting silver sulfide (Ag_2S) by Iso-Analytical Laboratories, Cheshire, UK, using standard EA-IRMS techniques, and reported in Yang *et al.* (2019). Minor S isotope analyses were conducted in the gas-source isotope geochemistry laboratory at the University of St Andrews, using a Curie-point pyrolysis sulfur fluorination line, as detailed in Warke *et al.* (2020).

The resulting sulfur isotope ratios ($^{33}S/^{32}S$, $^{34}S/^{32}S$, $^{36}S/^{32}S$) are reported using the standard delta notation (δ) showing per mil (‰) deviations from international standard V-CDT, as follows:

$$\delta^{3X}S\ (‰) = [{}^{3X}S/{}^{32}S_{sample}/{}^{3X}S/{}^{32}S_{V\text{-}CDT} - 1] \times 1000 \quad \text{(Eq. S-1)}$$

where ^{3X}S is ^{33}S, ^{34}S, or ^{36}S. Minor S isotope values are further expressed using $\Delta^{33}S$ and $\Delta^{36}S$ notation, calculated as:

$$\Delta^{33}S\ (‰) = \delta^{33}S - [({}^{34}S/{}^{32}S_{sample}/{}^{34}S/{}^{32}S_{V\text{-}CDT})^{0.515} - 1] \quad \text{(Eq. S-2)}$$

$$\Delta^{36}S\ (‰) = \delta^{36}S - [({}^{34}S/{}^{32}S_{sample}/{}^{34}S/{}^{32}S_{V\text{-}CDT})^{1.90} - 1]. \quad \text{(Eq. S-3)}$$

Long-term reproducibility of this method based on repeat analyses of IAEA-S1 (n = 75) is 0.014‰ for $\Delta^{33}S$ and 0.190‰ for $\Delta^{36}S$.

Total Hg concentrations were determined by the RA-915+ Hg analyzer coupled with the PYRO-915+ attachment (Lumex, Russia), at the Institute of Geochemistry, Chinese Academy of Sciences (IGCAS). Recoveries for standard reference material GSS-5 (n=3) were between 90 and 110 %, and coefficients of variation (triplicate analyses) were < 10 %. A double-stage tube furnace coupled with 5 mL of 40 % acid mixture (HNO3/HCl = 2/1, v/v) was used for preconcentration of Hg for isotope analysis (Deng *et al.*, 2021). The preconcentrated solutions were diluted to 0.5 ng/mL Hg and measured and analysed by Neptune Plus multi-collector inductively coupled plasma mass spectrometer (Thermo Electron Corp, Bremen, Germany) at IGCAS, following a previous method (Yin *et al.*, 2016). Mercury isotopes were expressed following conventional notation (Bergquist and Blum, 2007), such that mass-dependent fractionation (MDF) was expressed as $\delta^{202}Hg$ (in ‰) referenced to the NIST SRM 3133 Hg standard (analyzed before and after each sample):

$$\delta^{202}Hg\ (‰) = [{}^{202}Hg/{}^{198}Hg_{sample}/{}^{202}Hg/{}^{198}Hg_{standard} - 1] \times 1000. \quad \text{(Eq. S-4)}$$

Mass independent fractionation of Hg isotopes is further expressed in permil (‰), using $\Delta^{199}Hg$ and $\Delta^{201}Hg$ notation for odd-number Hg-MIF, and $\Delta^{200}Hg$ notation for even-number Hg-MIF, calculated as:

$$\Delta^{xxx}Hg\ (‰) = \delta^{xxx}Hg - \delta^{202}Hg \times \beta \quad \text{(Eq. S-5)}$$

where β is equal to 0.2520 for ^{199}Hg, 0.5024 for ^{200}Hg, and 0.7520 for ^{201}Hg. NIST-3177 secondary standard solutions, diluted to 0.5 ng/mL Hg with 10% HCl, were measured every 10 samples. The overall average and uncertainty of NIST-3177 and GSS-5 (Table S-3) agree well with previous results (Blum and Bergquist, 2007; Deng *et al.*, 2021). Uncertainties reported in this study (Table S-2) correspond to the larger value of either the measurement uncertainty of replicate digests of GSS-5 or the uncertainty of repeated measurements of UM-Almadén.

Supplementary Tables

Table S-1 Sulfur isotope data for the Manjeri Formation, given in ‰ relative to V-CDT. $\delta^{34}S$ values are as reported in Yang *et al.* (2019). Errors shown (1σ) are for individual measurements.

Sample	Member	Depth (m)	$\delta^{34}S$	$\Delta^{33}S$	1σ	$\Delta^{36}S$	1σ
B1-1	Jimmy	61.5	-10.3	-0.353	0.022	0.440	0.146
B2-1	Jimmy	63.31	-11.2	-0.365	0.012	0.537	0.151
B2-3	Jimmy	65.2	-7.1	0.881	0.023	-0.862	0.312
B2-11	Jimmy	65.35	-6.6	1.183	0.014	-2.486	0.134
B2-15	Jimmy	67.06	-5.5	1.407	0.022	-1.553	0.094
B2-18	Jimmy	68.14	-11.8	1.145	0.008	-1.527	0.091
B2-20	Jimmy	69.16	-8.0	0.381	0.019	-0.034	0.151
B3-02	Jimmy	70.72	-11.1	0.358	0.023	-0.121	0.160
B3-03	Jimmy	71.75	-3.0	0.951	0.029	-0.494	0.178
B3-13	Jimmy	72.5	3.4	2.190	0.014	-2.202	0.117
B3-14	Jimmy	73.15	1.4	2.509	0.023	-2.293	0.181
B3-17	Jimmy	74.74	2.4	2.715	0.020	-2.519	0.138
B4-19	Jimmy	75.58	-18.0	1.690	0.032	-0.631	0.196
B4-9	Jimmy	77.53	3.1	2.634	0.016	-2.493	0.08
B4-12	Jimmy	79.35	3.3	2.826	0.013	-3.372	0.044
B4-15	Jimmy	80.65	4.0	3.188	0.014	-3.130	0.105
B4-07	Jimmy	83.1	4.5	3.024	0.018	-3.102	0.121
B4-20	Jimmy	83.32	3.8	2.930	0.032	-1.956	0.18
B4-08	Jimmy	84.13	-9.3	1.645	0.037	-0.167	0.233
A7-6	Jimmy	102.65	-4.7	0.444	0.008	-0.268	0.105
A7-8	Jimmy	103.85	-7.4	0.469	0.014	-0.556	0.129
A7-7	Jimmy	103	-5.4	0.397	0.009	-0.365	0.150
A8-3	Jimmy	108.58	-1.5	1.124	0.015		
A7-3	Jimmy	104.48	-33.7	-0.169	0.020	1.441	0.179
A8-14	Jimmy	110.41	-2.3	0.497	0.016	-0.463	0.09
A7-4	Jimmy	105.53	-2.1	1.266	0.015	-1.267	0.161
A8-16	Jimmy	113	-0.9	0.575	0.014	-0.230	0.105
A8-2	Jimmy	107.53	0.3	1.504	0.013	-1.321	0.089
A8-5	Jimmy	110.8	-0.7	0.472	0.016	-0.121	0.114
A8-4	Jimmy	109.75	-0.7	0.679	0.012	-0.487	0.132
N-28	Shavi	136.4	1.3	-0.107	0.018	0.005	0.092
N-27	Shavi	136.85	1.3	-0.159	0.011		
N-65	Shavi	137.75	-2.5	-0.735	0.018	1.327	0.114
N-24	Shavi	139.48	-5.7	-1.263	0.016	1.571	0.075
N-23	Shavi	140.5	-0.6	-0.889	0.018	1.435	0.144
N-21	Shavi	142.32	2.2	-1.512	0.019	1.648	0.061
N-18	SV	151.6	5.1	-0.735	0.024	0.685	0.177
N-17	SV	152	4.6	-0.769	0.013	0.723	0.284
N-16	SV	153.1	2.6	-0.898	0.036	0.726	0.115
N-13	SV	161	4.5	-0.112	0.016	0.342	0.131
N-84	SV	159.8	3.1	-0.012	0.037		
N-88	SV	162.1	3.1	-0.076	0.019	0.751	0.150
N-12	SV	162.9	1.2	-0.318	0.016	0.527	0.118
N-11	SV	164.46	4.0	-0.208	0.009	0.760	0.133
N-10	SV	166.63	2.4	-0.360	0.013	0.404	0.066

Table S-2 Mercury concentrations, total organic carbon (TOC; as reported in Yang *et al.*, 2019), calculated Hg/TOC, and Hg isotope data (in ‰) for the Manjeri Formation. Uncertainties (2σ) were 0.12 ‰ for δ^{202}Hg, 0.06 ‰ for Δ^{199}Hg, 0.05 ‰ for Δ^{200}Hg, and 0.08 ‰ for Δ^{201}Hg.

Sample	Member	Depth (m)	TOC (wt%)	Hg (ppb)	Hg/ TOC	δ^{202}Hg	Δ^{199}Hg	Δ^{200}Hg	Δ^{201}Hg
B1-1	Jimmy	61.5	0.8	165	198	-3.49	0.09	0.01	0.00
B2-1	Jimmy	63.31	0.5	122	239	-4.18	0.11	0.04	0.08
B2-3	Jimmy	65.2	0.7	48	65	-3.57	0.10	-0.01	0.04
B2-11	Jimmy	65.35		25		-2.20	0.10	-0.02	0.06
B2-15	Jimmy	67.06		14		-1.06	0.11	0.04	0.04
B2-18	Jimmy	68.14		25		-2.56	0.14	0.02	0.10
B2-20	Jimmy	69.16		29		-0.97	0.01	-0.02	0.04
B3-02	Jimmy	70.72	0.3	47	142	-3.73	0.10	0.01	0.05
B3-03	Jimmy	71.75	0.5	42	89	-3.39	0.05	0.00	0.02
B3-13	Jimmy	72.5		18		-2.47	0.05	-0.03	0.01
B3-14	Jimmy	73.15		12		-0.40	0.08	0.02	0.08
B3-17	Jimmy	74.74		11		-0.47	0.11	0.01	0.04
B4-19	Jimmy	75.58		10		-1.12	0.10	-0.01	0.02
B4-9	Jimmy	77.53		17		-3.03	0.15	-0.02	0.03
B4-12	Jimmy	79.35		3		-2.64	0.14	0.07	0.08
B4-15	Jimmy	80.65		12		-1.85	0.11	0.08	0.03
B4-07	Jimmy	83.1	0.4	55	148	-4.01	0.07	-0.02	0.01
B4-20	Jimmy	83.32		4		-1.51	0.02	-0.01	0.02
B4-08	Jimmy	84.13	0.4	12	32	-2.92	0.07	0.04	0.05
A7-6	Jimmy	102.65	0.8	10	13	-1.64	0.14	0.06	0.08
A7-7	Jimmy	103		12		-1.69	0.15	0.05	0.07
A7-8	Jimmy	103.85	0.6	9	15	-0.90	0.07	0.03	0.01
A7-3	Jimmy	104.48	0.6	31	49	-3.74	0.16	0.03	0.07
A7-4	Jimmy	105.53	0.5	24	45	-3.79	0.16	0.07	0.13
A8-2	Jimmy	107.53	0.5	157	310	-4.16	0.13	0.02	0.06
A8-3	Jimmy	108.58		22		-4.15	0.11	-0.02	0.04
A8-4	Jimmy	109.75	0.3	30	96	-3.16	0.08	0.01	0.04
A8-14	Jimmy	110.41		11		-1.29	0.09	0.01	0.05
A8-5	Jimmy	110.8	0.2	26	147	-3.43	0.11	0.03	0.06
A8-16	Jimmy	113		17		-1.70	0.08	0.06	0.07
N-28	Shavi	136.4	1.4	2066	1455	0.63	-0.05	0.01	-0.06
N-27	Shavi	136.85	1.3	2050	1627	1.02	-0.09	0.01	-0.12
N-65	Shavi	137.75		962		0.90	-0.07	-0.01	-0.05
N-24	Shavi	139.48	0.7	585	790	0.24	-0.02	0.00	-0.04
N-23	Shavi	140.5		1586		-0.11	-0.12	-0.02	-0.12
N-21	Shavi	142.32	0.7	1026	1487	-0.26	0.02	0.02	-0.03
N-18	SV	151.6	0.5	505	1075	0.55	-0.06	-0.01	-0.09
N-17	SV	152		492		-0.05	0.04	0.04	-0.02
N-16	SV	153.1		475		-0.88	0.02	0.02	0.00
N-84	SV	159.8		418		-0.97	0.05	0.03	0.00
N-13	SV	161	0.2	172	781	-1.14	0.03	-0.01	0.02
N-88	SV	162.1		99		-0.33	0.03	0.01	-0.02
N-12	SV	162.9	0.2	66	388	-0.38	0.02	0.02	0.02
N-11	SV	164.46	0.2	271	1503	-1.83	0.06	0.04	0.06
N-10	SV	166.63	0.2	447	2355	-0.26	-0.03	0.00	-0.04

Table S-3 Hg isotope values (in ‰) of NIST-3177 and GSS-4.

	THg (ng/mL)	δ^{202}Hg	δ^{202}Hg	δ^{202}Hg	δ^{202}Hg	Δ^{199}Hg	Δ^{200}Hg
3177-1	0.5	-0.14	-0.26	-0.35	-0.55	-0.01	0.01
3177-2	0.5	-0.11	-0.29	-0.47	-0.61	0.04	0.02
3177-3	0.5	-0.18	-0.33	-0.44	-0.57	-0.04	-0.04
3177-4	0.5	-0.13	-0.23	-0.39	-0.46	-0.01	0
3177-5	0.5	-0.14	-0.29	-0.48	-0.58	0.01	0
3177-6	0.5	-0.11	-0.2	-0.36	-0.48	0.02	0.04
3177-7	0.5	-0.17	-0.26	-0.42	-0.5	-0.04	-0.01
3177-8	0.5	-0.1	-0.25	-0.42	-0.47	0.01	-0.02
Average		**-0.14**	**-0.26**	**-0.42**	**-0.53**	**0**	**0**
2SD		**0.06**	**0.08**	**0.1**	**0.12**	**0.06**	**0.05**
GSS-4-1	0.5	-0.8	-0.79	-1.61	-1.69	-0.38	0.02
GSS-4-2	0.5	-0.87	-0.87	-1.68	-1.77	-0.43	-0.02
GSS-4-3	0.5	-0.82	-0.8	-1.64	-1.69	-0.39	0.03
Average		**-0.83**	**-0.82**	**-1.65**	**-1.72**	**-0.4**	**0.01**
2SD		**0.07**	**0.08**	**0.08**	**0.09**	**0.05**	**0.05**

Supplementary Figures

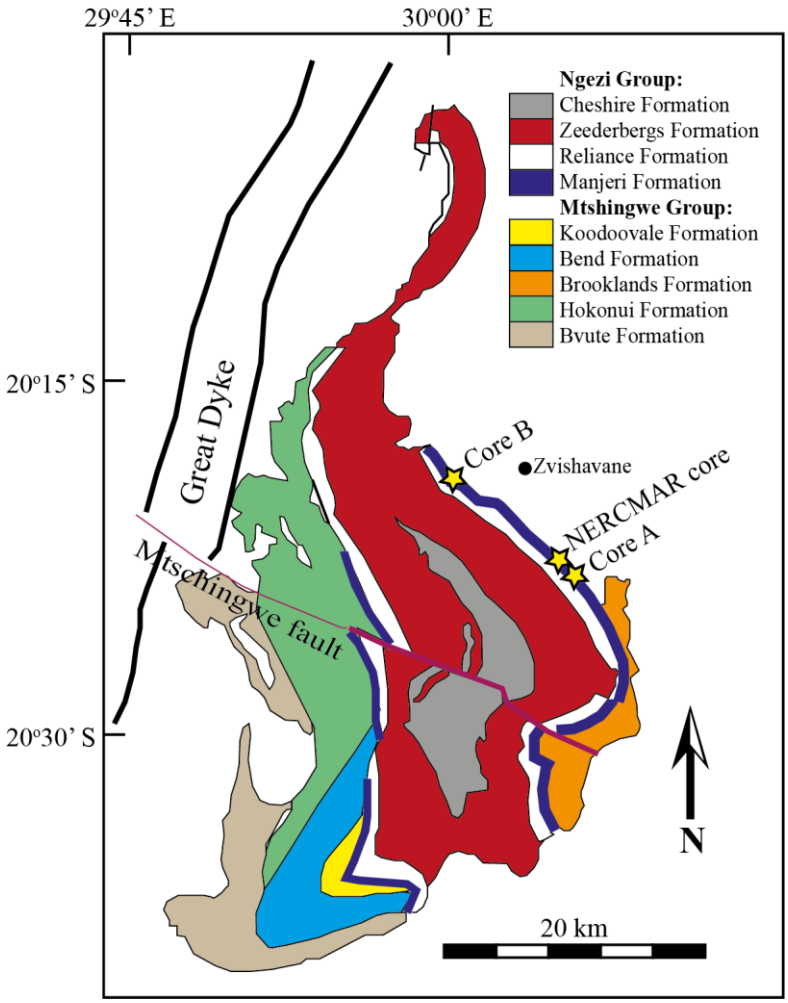

Figure S-1 Simplified geological map of the Belingwe Greenstone Belt, showing locations of the NERCMAR core, Core A and Core B (modified from Thomazo *et al.*, 2013).

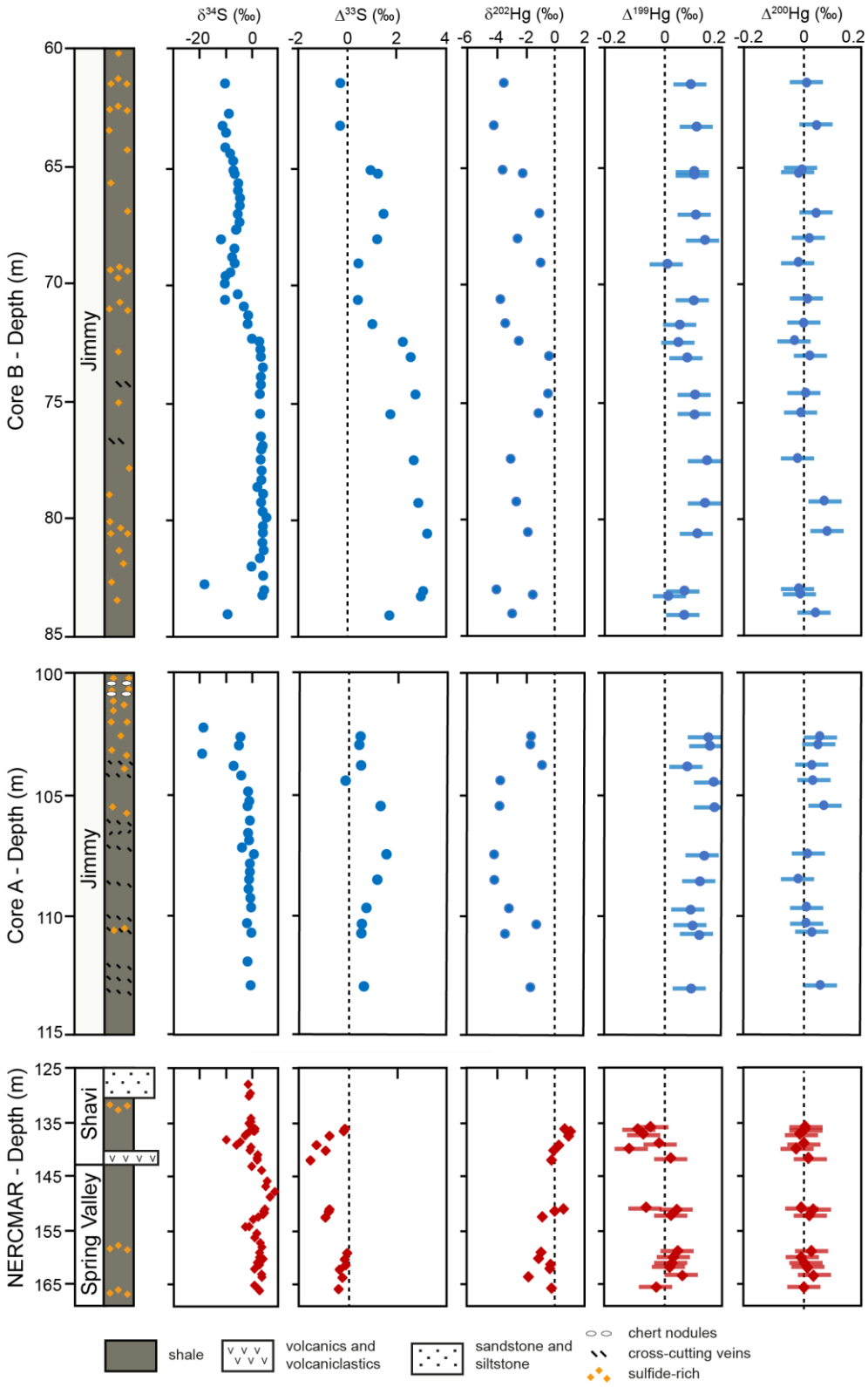

Figure S-2 Sulfur and mercury isotope data, plotted alongside core stratigraphy. Details of stratigraphic units and $\delta^{34}S$ data were previously reported in Yang *et al.* (2019).

Supplementary Information References

Bergquist, B.A., Blum, J.D. (2007) Mass-dependent and -independent fractionation of Hg isotopes by photoreduction in aquatic systems. *Science* 318, 417-420.

Blum, J.D., Bergquist, B.A. (2007) Reporting of variations in the natural isotopic composition of mercury *Analytical and Bioanalytical Chemistry* 388, 353-359.

Bolhar, R., Hofmann, A., Woodhead, J., Hergt, J., Dirks, P. (2002) Pb- and Nd-isotope systematics of stromatolitic limestones from the 2.7 Ga Ngezi Group of the Belingwe Greenstone Belt: constraints on timing of deposition and provenance. *Precambrian Research* 114, 277-294.

Deng, C., Sun, G., Rong, Y., Sun, R., Sun, D., Lehmann, B., Yin, R. (2021) Recycling of mercury from the atmosphere-ocean system into volcanic-arc-associated epithermal gold systems. *Geology* 49, 309-313.

Grassineau, N.V., Abell, P., Appel, P.W.U., Lowry, D., Nisbet, E.G. (2006) Early life signatures in sulfur and carbon isotopes from Isua, Barberton, Wabigoon (Steep Rock) and Belingwe Greenstone Belts (3.8 to 2.7 Ga). *Geological Society of America Memoirs* 198, 33-52.

Izon, G., Zerkle, A.L., Zhelezinskaia, I., Farquhar, J., Newton, R.J., Poulton, S.W., Eigenbrode, J.L., Claire, M.W. (2015) Multiple oscillations in Neoarchean atmospheric chemistry. *Earth and Planetary Science Letters* 431, 264-273.

Nisbet, E.G., Arndt, N.T., Bickle, M.J., Cameron, W.E., Chauvel, C., Cheadle, M., Hegner, E., Kyser, T.K., Martin, A., Renner, R., Roedder, E. (1987) Uniquely fresh 2.7 Ga komatiites from the Belingwe greenstone belt, Zimbabwe. *Geology* 15, 1147-1150.

Thomazo, C., Grassineau, N.V., Nisbet, E.G., Peters, M., Strauss, H. (2013) Multiple sulfur and carbon isotope composition of sediments from the Belingwe Greenstone Belt (Zimbabwe): A biogenic methane regulation on mass independent fractionation of sulfur during the Neoarchean? *Geochimica et Cosmochimica Acta* 121, 120-138.

Warke, M.R., Di Rocco, T., Zerkle, A.L., Lepland, A., Prave, A.R., Martin, A., Ueno, Y., Condon, D.J., Claire, M. (2020) The Great Oxidation Event preceded a Paleoproterozoic "snowball Earth". *PNAS* 117, 13314-13320.

Yang, J., Junium, C.K., Grassineau, N.V., Nisbet, E.G., Izon, G., Mettam, C., Martin, A., Zerkle, A.L. (2019) Ammonium availability in the Late Archaean nitrogen cycle. *Nature Geoscience* 12, 553-557.

Yin, R., Krabbenhoft, D.P., Bergquist, B.A., al., e. (2016) Effects of mercury and thallium concentrations on high precision determination of mercury isotopic composition by Neptune Plus multiple collector inductively coupled plasma mass spectrometry. *Journal of Analytical Atomic Spectrometery* 31, 2060-2068.